A high performance fiber-shaped PEDOT@MnO_2// C@Fe_3O_4 asymmetric supercapacitor for wearable electronics†

Jinfeng Sun,[a] *Yan Huang,*[b] *Chenxi Fu,*[b] *Yang Huang,*[b] *Minshen Zhu,*[b] *Xiaoming Tao,*[*a] *Chunyi Zhi**[bc] *and Hong Hu**[a]

[a] *Institute of Textiles and Clothing, The Hong Kong Polytechnic University, 11 Hong Chong Road, Hong Kong, China. E-mail: hu.hong@polyu.edu.hk; xiaoming.tao@polyu.edu.hk*

[b] *Department of Physics and Materials Science, City University of Hong Kong, 83 Tat Chee Avenue, Hong Kong, China. E-mail: cy.zhi@cityu.edu.hk*

[C] *Shenzhen Research Institute, City University of Hong Kong, Shenzhen 518000, China*

Abstract

Fiber-shaped supercapacitors, which are energy-storage devices that feature flexibility and wearability, could realize further gains in energy-storage performance if their electrodes are properly designed. Herein, we present a high energy-performance and flexible fiber-shaped supercapacitor by using PEDOT@MnO_2 and C@Fe_3O_4 composites as the positive and negative electrodes, respectively. The as-fabricated fiber-shaped supercapacitor with a high working voltage of 2 V exhibits a high areal specific capacitance of 60 mF cm^{-2} and a large energy density of 0.0335 mW h cm^{-2}. This fiber-shaped supercapacitor exhibits good flexibility and particularly can be deformed without energy-performance decay. Furthermore, this fiber-shaped supercapacitor woven into a wristband in series can successfully power a LED,

indicating its promising practical application in wearable electronics.

Introduction

The design of wearable electronic devices, such as sensors, nanogenerators and transistors, requires highly flexible energy storage devices as a power source.[1–3] Supercapacitors, with a long life cycle (>10^5 cycles), high power density (up to 10 kW kg^{-1}), and excellent safety, have been considered as the most promising power source for wearable electronic devices.[4,5] Compared with the traditional 2-D planar structured supercapacitors, fiber-shaped devices are particularly intriguing due to their excellent flexibility and deformability. Recently, fiber-shaped supercapacitors have undergone fast and extensive development.[6–10] It is expected that these devices could meet the requirements of future wearable electronic systems and can be easily woven or knitted into any desired shape. Although various fiber-shaped supercapacitors that have been developed exhibited high flexibility, their simple, efficient and scalable fabrication still presents a major challenge if their practical applications are to be fully realized.

In terms of selection of electrode materials, there are primarily two types of fiber-shaped supercapacitors: symmetrical and asymmetrical. Symmetric fiber supercapacitors usually use the same material (carbon materials or conductive polymers) in electrode fabrication. However, the symmetric-type cell has a limited operating working potential range from 0.6 to 1 V, and thus only relatively low energy density is achieved according to the equation, $E = 1/2CV^2$. [11] Most reported symmetric fiber supercapacitors display an energy density in a range of 10^{-4} to 10^{-2} mW h cm^{-2} , which cannot meet the requirement of practical applications.[12–14] Asymmetric supercapacitors (ASCs), which combine a faradaic redox electrode and a capacitor-type electrode, can deliver a large energy density as a result of extending the effective voltage window up to 2 V in aqueous electrolytes and blending the great specific capacity of the faradaic redox electrode.[15] Furthermore, ASCs can maintain fast charge/discharge rates due to the usage of capacitive-type electrodes. According to the working principle of ASCs, an appropriate electrode combination can even increase both the working voltage and rate capability, further contributing to the improvement of the energy and power densities. Recently, extensive studies have been devoted to building numerical ASCs, such as rGO-RuO_2//rGO–PANi, $Ni(OH)_2$–graphene//graphene, MnO_2//graphene, flower-like $Co(OH)_2$// urchin-like VN, MnO_2@TiN//EACC, MoS_2–rGO/MWCNT//rGO/MWCNT, MnO_2//WON–ASCs, GF/CNT/MnO_2//GF/CNT/Ppy, and CoO@PPy//AC.[16–24] Although these ASCs have made great progress in improving the energy/power performance, most of these asymmetric configurations are realized based on the traditional planar design. Therefore, an efficient and systematic design to improve both the energy and power densities of fiber supercapacitors presents a major challenge in accelerating the practical applications of wearable electronics.

Stainless steel yarns, fabricated by using twist-bundledrawing multiple high-temperature thin fibers together, with super strength, excellent flexibility and conductivity can be considered as an excellent candidate in the form of the current collector or scaffold for electro-active materials. Herein, PEDOT@MnO_2 and C@Fe_3O_4 nanostructures were directly grown on the conductive yarn, serving as the positive and negative electrodes, respectively. The assembled yarn ASC operates within a high working potential up to 2 V, yielding a high areal and volumetric capacitance of 60 mF cm^{-2} and 7.2 F cm^{-3} at a current of 0.9 mA and a good rate capability. At a power density of 0.6 mW cm^{-2} (72 mW cm^{-3}), the hybrid device achieved a high energy density of 0.0335 mW h cm^{-2} and 4.02 mW h cm^{-3} , so far, among the highest values reported for fiber-shaped supercapacitors.

Method

Synthesis of PEDOT/MnO_2 and C/FeO electrodes

The PEDOT@MnO_2 composite electrode was fabricated by a two-step electrodeposition process. MnO_2 was first electrochemically deposited on a stainless steel fiber directly in 0.25 M $Mn(NO_3)_2$ aqueous solution at 0.6 V vs. SCE for 1C. After that, the resultant yarn was further electrodeposited with PEDOT at 1 V vs. SCE for 60 s in a solution of 0.07 M sodium dodecyl sulfate (SDS), 0.1 M $LiClO_4$ and 0.05 M 3,4-ethoxylene dioxythiophene (EDOT) at room temperature. The total mass of the PEDOT@MnO_2 composite was 1.27 mg.

To synthesize a C@Fe_3O_4 electrode, a stainless steel fiber was electrodeposited with

Fe_3O_4 in a $(NH_4)_2Fe(SO_4)_2$ and KCH_3COO solution at a constant voltage of 0.65 V for 1.2 C at 70 C. Afterwards, PEDOT was electrodeposited through the same method mentioned above. Finally, the as-prepared PEDOT@Fe_3O_4 electrode was annealed at 500 C for 3 h in Ar to obtain the C@Fe_3O_4 electrode. The total mass of the C@Fe_3O_4 composite was 1.42 mg.

Material characterization

Field emission scanning electron microscopy (FESEM, JSM 7800F, JEOL, Japan) and scanning electron microscopy (SEM, Leica Stereoscan 440) were employed to investigate the surface morphologies of the as-prepared samples. Powder X-ray diffraction (XRD, Rigaku D/Max-2400, Japan) was performed using Cu-Ka radiation to investigate the structure and composition of the samples. Raman spectra of the samples were recorded using a micro-Raman spectroscope (JY-HR800, the excitation wavelength is 532 nm).

Electrochemical characterization of individual electrodes

Capacitance measurements were performed in 1 M LiCl aqueous electrolyte in a 3-electrode cell setup with a CHI 760E electrochemical workstation. A single yarn, an SCE electrode, and a large-area Pt foil served as the working, the reference, and the counter electrodes, respectively. Electrochemical impedance spectra (EIS) were measured at frequencies ranging from 0.01 Hz to 100 kHz with a potential amplitude of 5 mV. All measurements were carried out at room temperature. Capacitances in the three-electrode cell were calculated according to ref. 25. In brief, the capacitance of the electrode (*C*) was calculated using the charge integrated from GCD and CV curves individually according to the formulas:

$$C = \frac{It}{U} \qquad (1)$$

$$C = \frac{1}{2Uv}\int_{U-}^{U+} i(U)dU \qquad (2)$$

where I is the discharge current during GCD, t is the discharge time during GCD, U is the voltage range, v is the scan rate of the CV curve, and $i(U)$ is the current during CV. The yarn is approximately considered to be a cylinder. The surface area ($S_{\text{electrode}}$) and volume ($V_{\text{electrode}}$) of the yarn were determined according to the formulas:

$$S_{\mathrm{electrode}} = \pi D L \quad (3)$$

$$V_{\mathrm{electrode}} = \pi(\frac{D}{2})^2 L \quad (4)$$

where D is the diameter of the yarn and L is the length of the yarn. The specific capacitances normalized to the area (C_A) were calculated by using the capacitance of the electrode C divided by the area $S_{\mathrm{electrode}}$.

Fabrication and electrochemical characterization of asymmetric supercapacitors

The PVA/LiCl electrolyte was prepared with 6 g LiCl, 6 g PVA and 60 mL deionized water at 90 °C. Two identical as-deposited yarns were immersed in the cooled electrolyte solution for 5 min. Thereafter, the electrolyte wetted yarns were placed in parallel and dried until gel solidification under ambient conditions. Finally, the solid-state supercapacitor was obtained with the electrolyte also serving as a separator. The performance of the assembled yarn supercapacitors was measured by CV and GCD in a two-electrode configuration. Power (P) and energy densities (E) of the yarn supercapacitor were individually calculated according to ref. 25.

$$E = \frac{1}{2} C U^2 \quad (5)$$

$$P = \frac{E}{t} \quad (6)$$

Results and discussion

Characterization of the positive electrode

The PEDOT@MnO_2 nanostructure was grown on the stainless steel fiber directly via an electrochemical deposition method. Scanning electron microscopy (SEM) images (Fig. 1 and S1†) of the resulting sample show that the stainless steel fibers surrounded by MnO_2 nanosheets are uniformly coated by PEDOT. Fig. 1d displays the Raman spectrum of the as-prepared samples. Compared to the pristine stainless steel yarn (Fig. S1c†), the MnO_2 deposited yarn has three typical peaks at 500 cm^{-1} , 560 cm^{-1} and 645 cm^{-1} in agreement with previously reported MnO_2. [26] Strong signals corresponding to PEDOT are observed, while Raman peaks of MnO_2 are reduced, further confirming that PEDOT was uniformly coated on the MnO_2 nanosheets. The corresponding XRD patterns of the samples are shown in Fig. S2,† exhibiting only peaks pertaining to the pristine stainless steel yarn. There are no obvious peaks of MnO_2, which are associated with the amorphous structure of deposited MnO_2 in nature.[27]

The electrochemical studies for the as-prepared PEDOT@MnO_2 electrode were conducted in a three-electrode configuration. A 10 cm yarn electrode (effective area ~0.785 cm^2) was dipped into 1 M LiCl solution at room temperature for a single electrode test. The SCE reference electrode and Pt plate counter electrode were used in the measurement. Fig. 2a and b show the cyclic voltammetry (CV) curves of the pristine MnO_2 and PEDOT@MnO_2 electrodes collected at different scan rates. As expected, the PEDOT@MnO_2 electrode exhibited a considerably larger current density than the pristine MnO_2 electrode, indicating a remarkable improvement of the electrochemical capacitance after PEDOT deposition. This can be attributed to the synergistic effect arising from MnO_2 and PEDOT nanostructures. The MnO_2 and PEDOT nanostructures are uniformly deposited hierarchical structures which will facilitate the fully utilized ionaccessible surface area of yarns.[13] Moreover, the MnO_2 nanostructure contributes predominately to the capacitance, and conducting PEDOT wrapped on the nonconductive MnO_2 nanostructure provides a better conductivity for electron transportation and also participates in the pseudocapacitive charge storage process. In addition, from the CV curves of the PEDOT@MnO_2 electrode, the intensity of the redox peaks increases with increasing sweep rate. Fig. 2c shows the charge-discharge (GCD) curves of the yarn electrode at different current densities. The nearly triangular shape of the GCD curves indicates the good reversibility behavior of the PEDOT@MnO_2 electrode.[28] The relationship between the calculated areal capacitance and discharge current density (Fig. 2d) indicates the excellent rate capability of the electrode, which led to a capacitance retention of 55% as the current increased from 1 to 5 mA.

Characterization of the negative electrode

The C@Fe_3O_4 electrode was synthesized via a two-step electrodeposition followed by a heat treatment process. First, the Fe_3O_4 precursor was electrodeposited directly on conductive yarn, exhibiting a nanosheet structure (Fig. 3a and b). After the PEDOT electrodeposition and heat treatment process, the surface of the yarn electrode becomes much smoother (Fig. 3c), indicating that a carbon layer was uniformly coated on the fiber. Raman spectroscopy was performed to gain insight into the chemical composition of the yarn electrode (Fig. 3d). The Raman spectrum of Fe_3O_4 shows characteristic peaks at 318, 540, and 665 cm^{-1} , corresponding to Fe3O4. [29] The absence of any further peaks in the Raman spectra indicates the formation of pure Fe_3O_4 on the conductive fiber. Except for the characteristic peaks of Fe3O4, the Raman spectrum of C@Fe_3O_4 shows strong broad peaks at 1490 and 2950 cm^{-1} , corresponding to amorphous carbon.[30,31] XRD results further confirm the as-prepared species (Fig. S3†). The generation of amorphous carbon can be attributed to the relatively low temperature treatment.[30,31]

Fig. 4 shows the electrochemical characterization of Fe_3O_4 and C@Fe_3O_4 coated fibers. Based on the direct proportion between capacitance and integral area of CV curves,[32,33] a significantly better performance of the C@Fe_3O_4 electrode compared to the Fe_3O_4 is clearly seen (Fig. 4a and b). This can be ascribed to the uniform coating of the C film on the Fe_3O_4 nanosheets. Typical GCD curves were plotted for the C@Fe_3O_4 electrode with various current densities (Fig. 4c). The nearly triangular shape of the GCD curves indicates its good reversibility behavior. Furthermore, capacitances were calculated from the corresponding galvanostatic discharge curves following the equation $C = It/U$ (Fig. 4d). The electrode delivers a discharge capacity of 127 mF cm^{-2} at a current of 1 mA and a specific capacity of 60.74 mF cm^{-2} at 8 mA, with a high capacity retention of 48%.

Solid-state asymmetric supercapacitor based on PEDOT@MnO_2 and C@Fe_3O_4 yarn electrodes

The solid-state yarn ASC was fabricated with PEDOT@MnO_2 as the positive electrode and C@Fe_3O_4 as the negative electrode using a gel electrolyte. In order to develop an optimal PEDOT@MnO_2//C@Fe_3O_4 asymmetric supercapacitor, a series of comparative experiments were conducted (ESI Fig. S4 and S5†). The optimal negative (1.42 mg)/positive (1.27 mg) mass ratio of 1.12 from experimental results is slightly less than the theoretical value of 1.4. This result is similar to previously reported studies which suggested that the maximum electrochemical value for ASCs was obtained at a lower positive/negative mass ratio (less than the q balance value).[19,34–36] Fig. 5 demonstrates the CV curves of the optimized yarn ASC collected at 100 mV s^{-1} and

GCD curves at a constant current of 1.8 mA with an operational voltage window ranging from 0.8 to 2 V. The CV curves maintained their shape as the applied voltage increased, indicating that the PEDOT@MnO_2//C@Fe_3O_4 ASC device is stable up to a high voltage of 2 V. Furthermore, specific capacitance as a function of the operating voltage window is displayed in Fig. S6.† The capacitance value increased with increasing voltage window. Thus, an operating voltage window of 0 to 2 V was selected for further electrochemical study of the yarn ASC.

CV curves of the solid-state ASC exhibit nearly rectangular shapes even with a scan rate up to 500 mV s^{-1} (Fig. 6a), suggesting a good reaction reversibility and excellent capacitive performance.[37] The specific capacitances of the yarn ASC calculated by length, area and volume are 10.97 mF cm^{-1} , 73.21 mF cm^{-2} and 8.78 F cm^{-3} at 20 mV s^{-1} , respectively. The GCD curves at different currents are shown in Fig. 6b. The coulombic efficiency of the assembled ASC is about 90%. This can be attributed to the further irreversible oxidation of the active materials at high voltage.[38–40] The quasi-triangular shapes further confirm the excellent capacitive performance of the PEDOT@MnO_2//C@Fe_3O_4 yarn ASC. Fig. 6c demonstrates the calculated capacitances based on the discharge curves. The yarn ASC achieved a high areal and volumetric capacitance of 60 mF cm^{-2} and 7.23 F cm^{-3} at a current of 0.9 mA and exhibited good rate performance with 65% retention of its original capacitance when the current was increased to 3.6 mA. It should be noted that the capacitance of the PEDOT@MnO_2//C@Fe_3O_4 yarn ASC exhibits a capacitance increase in the first 50 cycles (Fig. 6d), which is attributed to the increased effective interfacial area between electrode materials and the solid-state electrolyte, as well as the full activation of the electrode.[41–43] A capacitance retention of 80% was obtained after 800 cycles. Most reported studies on Mn// Fe ASCs or batteries suggested that the capacitance decay may be related to the structural change caused by the mechanical expansion of active materials during the ion insertion/deinsertion process or active-material detachment from the electrode.[44–46] From electrochemical impedance spectroscopy (EIS) measurements (Fig. 6e), the internal resistance, which intercepted with the real axis at high frequency, is 6 Ω. [47] The semicircle in the high frequency region represents the charge transfer resistance of the yarn supercapacitor.[48] The solid electrolytes always bring ion-transfer issues which induce a larger resistance of solid-state yarn supercapacitors compared to normal supercapacitor devices.[49] Despite this, the value of our yarn supercapacitor is much smaller than previously reported values.[50,51]

Energy and power densities are two important parameters to evaluate the energy storage performance of supercapacitor devices. The total length, area and volume of the fabricated yarn supercapacitor were estimated to be 10 cm, 1.5 cm^2 and 0.0125 cm^3 , respectively. Fig. 6d displays the Ragone plots of our yarn supercapacitor compared with recently reported flexible yarn supercapacitors. A high energy density of 0.005 mW h cm^{-1} , 0.0335 mW h cm^{-2} and 4.02 mW h cm^{-3} was obtained based on the discharge curves, respectively, which is considerably higher than those of previously reported solid-state yarn supercapacitors, such as SWCNT/PANiNW fiber supercapacitors by wet spinning (0.00056 mW h cm^{-2}),[52] rGO–Ni–yarn supercapacitor (0.0016 mW h cm^{-2}),53 coaxial wet-spun yarn supercapacitors (0.00348 mW h cm^{-2}),54 MnO2@TiN//N–MoO_{3-x} fiber ASC (2.29 mW h cm^{-3}),[55] and the PEDOT/CNT yarn supercapacitor (1.4 mW h cm^{-3}),[56] and is still comparable with that of all carbon solid-state yarn supercapacitor (0.0065 mW h cm^{-1}).[57]

In order to demonstrate the flexibility of our ASC device, a CV test was conducted at different deformations, such as bending, knotting and winding (Fig. 7a). As shown in Fig. 7b, the deformations have no obvious influence on the performance of the yarn supercapacitor, revealing the remarkable flexibility of the solid-state ASC device. Furthermore, two ASC devices, connected in series and knitted into a fabric, successfully drive a LED (Fig. 7c).

Conclusion

In summary, we have successfully constructed a wearable, fiber-shaped ASC with a high working voltage of 2 V. PEDOT@MnO_2 and C@Fe_3O_4 composites were directly coated on the stainless steel yarn to serve as the positive and negative electrodes, respectively. With the use of a highly flexible, conductive yarn substrate, the obtained yarn ASC shows good flexibility and can be deformed without performance decay. Furthermore, the ASC exhibits an excellent areal specific capacitance of 60 mF cm^{-2}

and an energy density of 0.0335 mW h cm^{-2} , making it a promising energy storage device for wearable electronic devices.

Acknowledgements

This work was supported by the Early Career Scheme of the Research Grants Council of Hong Kong SAR, China (CityU 109213), the Science Technology and Innovation Committee of Shenzhen Municipality (JCYJ20140419115507579) and the Hong Kong Polytechnic University (1-BBA3).

References

1 W. Zeng, L. Shu, Q. Li, S. Chen, F. Wang and X. Tao, Adv. Mater., 2014, 26, 5310–5336.

2 Q. Meng, H. Wu, Y. Meng, K. Xie, Z. Wei and Z. Guo, Adv. Mater., 2014, 26, 4100–4106.

3 Y. Shao, M. F. El-Kady, L. J. Wang, Q. Zhang, Y. Li, H. Wang, M. F. Mousavi and R. B. Kaner, Chem. Soc. Rev., 2015, 44, 3639–3665.

4 Z. Hu, X. Xiao, C. Chen, T. Li, L. Huang, C. Zhang, J. Su, L. Miao, J. Jiang, Y. Zhang and J. Zhou, Nano Energy, 2015, 11, 226.

5 R. Bendi, V. Kumar, V. Bhavanasi, K. Parida and P. S. Lee, Adv. Energy Mater., 2016, 6, 1501833.

6 L. Liu, Y. Yu, C. Yan, K. Li and Z. Zheng, Nat. Commun., 2015, 6, 7260.

7 Z. Yu, J. Moore, J. Calderon, L. Zhai and J. Thomas, Small, 2015, 11, 5289–5295.

8 B. Wang, X. Fang, H. Sun, S. He, J. Ren, Y. Zhang and H. Peng, Adv. Mater., 2015, 27, 7854–7860.

9 G. Qu, J. Cheng, X. Li, D. Yuan, P. Chen, X. Chen, B. Wang and H. Peng, Adv. Mater., 2016, 28, 3646–3652.

10 N. Liu, W. Ma, J. Tao, X. Zhang, J. Su, L. Li, C. Yang, Y. Gao, D. Golberg and Y. Bando, Adv. Mater., 2013, 25, 4925–4931.

11 Y. Zeng, Y. Han, Y. Zhao, Y. Zeng, M. Yu, Y. Liu, H. Tang, Y. Tong and X. Lu, Adv. Energy Mater., 2015, 5, 1402176.

12 S. T. Senthilkumar, Y. Wang and H. Huang, J. Mater. Chem. A, 2015, 3, 20863–20879.

13 Y. Huang, H. Hu, Y. Huang, M. Zhu, W. Meng, C. Liu, Z. Pei, C. Hao, Z. Wang and C. Zhi, ACS Nano, 2015, 9, 4766–4775.

14 D. Yu, Q. Qian, L. Wei, W. Jiang, K. Goh, J. Wei, J. Zhang and Y. Chen, Chem. Soc. Rev., 2015, 44, 647–662.

15 M. Yu, Z. Wang, Y. Han, Y. Tong, X. Lu and S. Yang, J. Mater. Chem. A, 2016, 4, 4634–4658.

16 J. Yan, Z. Fan, W. Sun, G. Ning, T. Wei, Q. Zhang, R. Zhang, L. Zhi and F. Wei, Adv. Mater., 2012, 22, 2632–2641.

17 J. Zhang, J. Jiang, H. Li and X. S. Zhao, Energy Environ. Sci., 2011, 4, 4009–4015.

18 S. Shi, C. Xu, C. Yang, Y. Chen, J. Liu and F. Kang, Sci. Rep., 2013, 3, 2598.

19 R. Wang, X. Yan, J. Lang, Z. Zheng and P. Zhang, J. Mater. Chem. A, 2014, 2, 12724–12732.

20 W. Wang, W. Liu, Y. Zeng, Y. Han, M. Yu, X. Lu and Y. Tong, Adv. Mater., 2015, 27, 3572–3578.

21 G. Sun, X. Zhang, R. Lin, J. Yang, H. Zhang and P. Chen, Angew. Chem., 2015, 127, 4734–4739.

22 M. Yu, Y. Han, X. Cheng, L. Hu, Y. Zeng, M. Chen, F. Cheng, X. Lu and Y. Tong, Adv. Mater., 2015, 27, 3085–3091.

23 J. Liu, L. Zhang, H. B. Wu, J. Lin, Z. Shen and X. W. (David) Lou, Energy Environ. Sci., 2014, 7, 3709–3719.

24 C. Zhou, Y. Zhang, Y. Li and J. Liu, Nano Lett., 2013, 13, 2078–2085.

25 Z. Weng, Y. Su, D.-W. Wang, F. Li, J. Du and H. –M. Cheng, Adv. Energy Mater., 2011, 1, 917–922.

26 A. Ogata, S. Komaba, R. Baddour-Hadjean, J. P. Pereira-Ramos and N. Kumagai, Electrochim. Acta, 2008, 53, 3084–3093.

27 K. Xiao, J.-W. Li, G.-F. Chen, Z.-Q. Liu, N. Li and Y. Z. Su, Electrochim. Acta, 2014, 149, 341–348.

28 D. Yu, K. Goh, H. Wang, L. Wei, W. Jiang, Q. Zhang, L. Dai and Y. Chen, Nat. Nanotechnol., 2014, 9, 555–562.

29 D. L. A. de Faria, S. V. Silva and M. T. de Oliveira, J. Raman Spectrosc., 1997, 28, 873–878.

30 J. Schwan, S. Ulrich, V. Batori, H. Ehrhardt and S. R. P. Silva, J. Appl. Phys., 1996,

80, 440–447.

31 P. K. Chu and L. Li, Mater. Chem. Phys., 2006, 96, 253–277. 32 T. Zhou, W. Pang, C. Zhang, J. Yang, Z. Chen, H. Liu and Z. Guo, ACS Nano, 2014, 8, 8323–8333.

33 C. Meng, C. Liu, L. Chen, C. Hu and S. Fan, Nano Lett., 2010, 10, 4025–4031.

34 J. P. Zheng, J. Electrochem. Soc., 2003, 150, A484–A492.

35 J. P. Zheng, J. Electrochem. Soc., 2009, 156, A500–A505.

36 G. A. Snook, G. J. Wilson and A. G. Pandolfo, J. Power Sources, 2009, 186, 216–223.

37 S. Sun, J. Lang, R. Wang, L. Kong, X. Li and X. Yan, J. Mater. Chem. A, 2014, 2, 14550–14556.

38 Z. Chen, V. Augustyn, X. Jia, Q. Xiao, B. Dunn and Y. Lu, ACS Nano, 2012, 6, 4319–4327.

39 A. Gambou-Boscaa and D. B´elanger, J. Mater. Chem. A, 2014, 2, 6463–6473.

40 G. Sun, X. Zhang, R. Lin, J. Yang, H. Zhang and P. Chen, Angew. Chem., 2015, 127, 4734–4739.

41 C. Long, T. Wei, J. Yan, L. Jiang and Z. Fan, ACS Nano, 2013, 7, 11325–11332.

42 C. Yuan, J. Li, L. Hou, X. Zhang, L. Shen and X. W. (David) Lou, Adv. Funct. Mater., 2012, 22, 4592–4597.

43 Z. Fan, J. Yan, L. Zhi, Q. Zhang, T. Wei, J. Feng, M. Zhang, W. Qian and F. Wei, Adv. Mater., 2010, 22, 3723–3728.

44 H. Wang, Z. Xua, H. Yia, H. Wei, Z. Guo and X. Wang, Nano Energy, 2014, 7, 86–96.

45 H. Wang, Y. Liang, M. Gong, Y. Li, W. Chang, T. Mefford, J. Zhou, J. Wang, T. Regier, F. Wei and H. Dai, Nat. Commun., 2012, 3, 917.

46 J. Liu, J. Wang, Z. Ku, H. Wang, S. Chen, L. Zhang, J. Lin and Z. X. Shen, ACS Nano, 2016, 10, 1007–1016.

47 M. F. El-Kady and R. B. Kaner, Nat. Commun., 2013, 4, 1475.

48 H. P. Cong, X. C. Ren, P. Wang and S. H. Yu, Energy Environ. Sci., 2013, 6, 1185–1191.

49 D. Yu, S. Zhai, W. Jiang, K. Goh, L. Wei, X. Chen, R. Jiang and Y. Chen, Adv. Mater., 2015, 27, 4895–4901.

50 C. Choi, S. H. Kim, H. J. Sim, J. A. Lee, A. Y. Choi, Y. T. Kim, X. Lepr´o, G. M.

Spinks, R. H. Baughman and S. J. Kim, Sci. Rep., 2015, 5, 9387.

51 H. Tang, J. Wang, H. Yin, H. Zhao, D. Wang and Z. Tang, Adv. Mater., 2015, 27, 1117–1123.

52 Q. Meng, K. Wang, W. Guo, J. Fang, Z. Wei and X. She, Small, 2014, 10, 3187–3193.

53 X. Pu, L. Li, M. Liu, C. Jiang, C. Du, Z. Zhao, W. Hu and Z. L. Wang, Adv. Mater., 2016, 28, 98–105.

54 L. Kou, T. Huang, B. Zheng, Y. Han, X. Zhao, K. Gopalsamy, H. Sun and C. Gao, Nat. Commun., 2014, 5, 3754.

55 M. Yu, X. Cheng, Y. Zeng, Z. Wang, Y. Tong, X. Lu and S. Yang, Angew. Chem., Int. Ed., 2016, 55, 6762–6766.

56 J. A. Lee, M. K. Shin, S. H. Kim, H. U. Cho, G. M. Spinks, G. G. Wallace, M. D. Lima, X. Lepr´o, M. E. Kozlov, R. H. Baughman and S. J. Kim, Nat. Commun., 2013, 4, 1970.

57 S. Zhai, W. Jiang, L. Wei, H. E. Karahan, Y. Yuan, A. K. Ng and Y. Chen, Mater. Horiz., 2015, 2, 598–605.

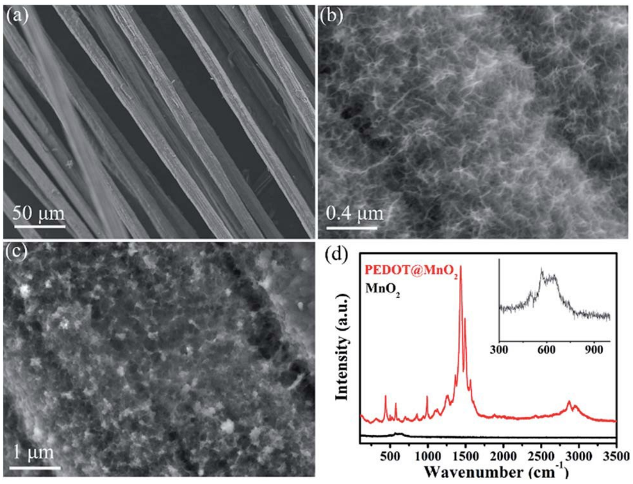

Fig. 1 (a) and (b) SEM images of MnO$_2$ on stainless steel fibers. (c) SEM image of PEDOT@MnO . (d) Raman spectra of MnO and PEDOT@MnO$_2$ (inset shows the magnified view of MnO$_2$ in the marked region).

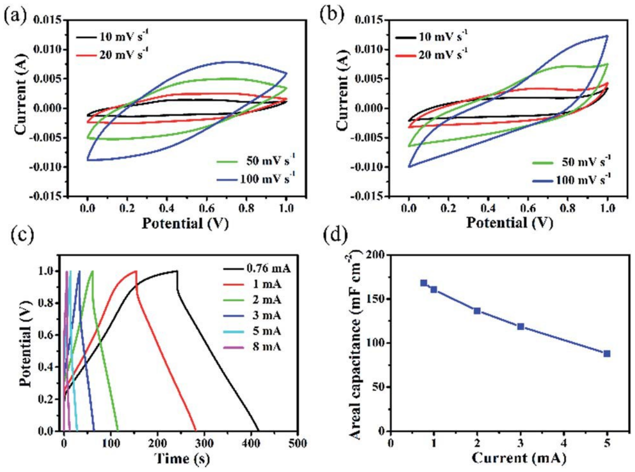

Fig. 2 Electrochemical performance of PEDOT@MnO$_2$ in a three electrode cell. (a) CV curves of pure MnO$_2$ at different scan rates from 10 to 100 mV s^{-1} within a potential range of 0 to 1.0 V (vs. SCE) in 1 M LiCl aqueous solution. (b) CV curves of the PEDOT@MnO$_2$ composite electrode at different scan rates from 10 to 100 mV s^{-1} . (c) Galvano-static charge and discharge curves of PEDOT@MnO$_2$ at different currents. (d) Specific capacitances of PEDOT@MnO$_2$ calculated from GCD data in (c).

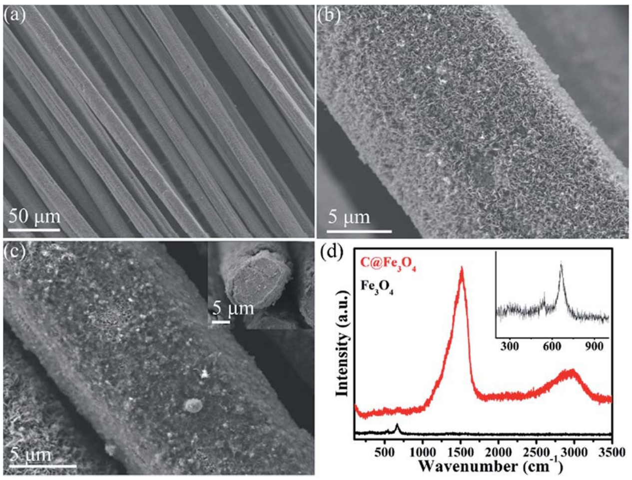

Fig. 3 (a) and (b) SEM images of Fe_3O_4 on a stainless steel fiber. (c) SEM images of C@Fe_3O_4; the inset is the cross-section of the C@Fe_3O_4 coated yarn. (d) Raman spectra of Fe_3O_4 and C@Fe_3O_4 (inset shows the magnified view of Fe_3O_4 in the marked region).

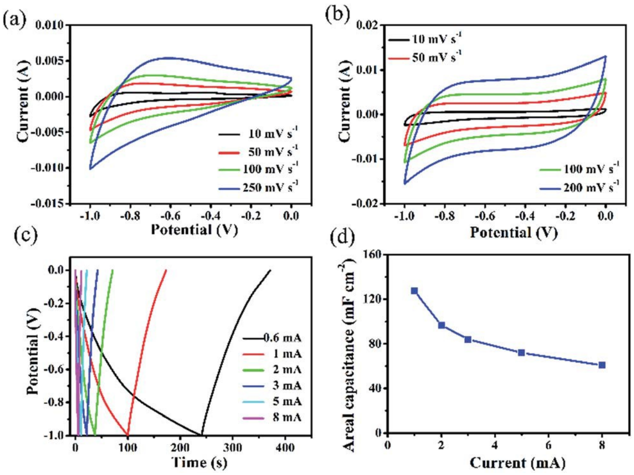

Fig. 4 Electrochemical performance of C@Fe_3O_4 in a three electrode cell. (a) CV curves of pure Fe_3O_4 at different scan rates from 10 to 250 mV s^{-1}. (b) CV curves of the C@Fe_3O_4 composite electrode at different scan rates from 10 to 200 mV s^{-1}. (c) GCD curves of C@Fe_3O_4 at different currents. (d) Areal specific capacitance of C@Fe_3O_4 calculated from GCD data in (c).

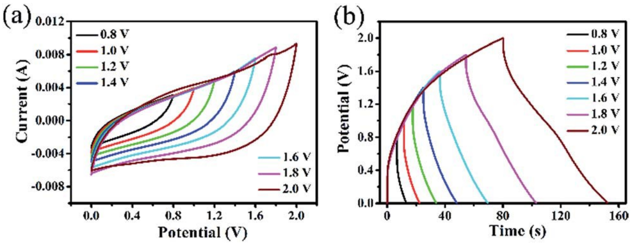

Fig. 5 (a) CV curves at 100 mV s^{-1} and (b) GCD curves at a constant current of 1.8 mA of the assembled solid-state ASC device collected at different voltage windows.

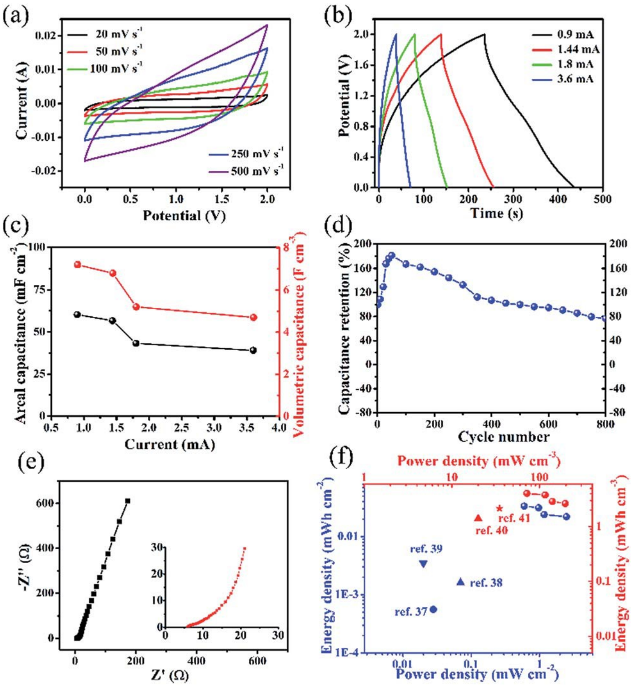

Fig. 6 (a) CV curves of the ASC device at various scan rates from 20 to 500 mV s^{-1}. (b) GCD curves of the ASC device at different currents. (c) Areal and volumetric capacitance at different currents. (d) Cycling performance of the ASC at a current of 80% for 800 cycles. (e) Nyquist plots of the yarn ASC. (f) Energy and power densities of the fabricated yarn ASC compared with recently reported yarn supercapacitors.

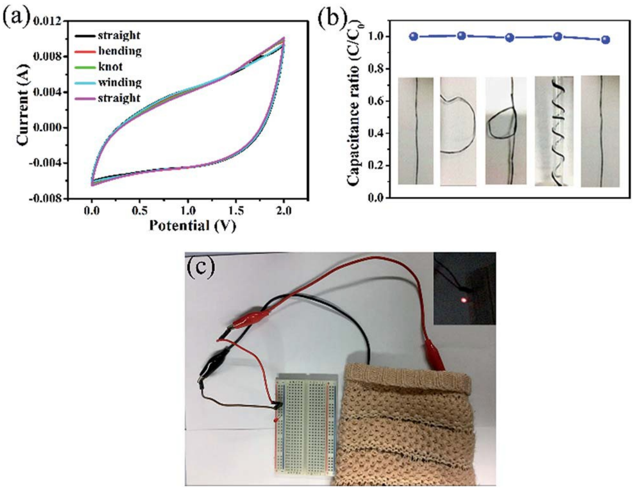

Fig. 7 Flexibility tests of the PEDOT@MnO_2//C@Fe_3O_4 yarn ASC. (a) CV curves of the yarn ASC undergoing different deformations at a scan rate of 100 mV s^{-1}. (b) Capacitance retention under various deformations. (c) Optical image of two 10

cm long PEDOT@MnO_2//C@Fe_3O_4 yarn ASCs fabricated in series and knitted into a wristband powering a LED.